

Visualizing the chiral anomaly in Dirac and Weyl semimetals with photoemission spectroscopy

Jan Behrends,¹ Adolfo G. Grushin,¹ Teemu Ojanen,² and Jens H. Bardarson¹

¹*Max-Planck-Institut für Physik komplexer Systeme, Nöthnitzer Str. 38, 01187 Dresden, Germany*

²*Low Temperature Laboratory, Department of Applied Physics, Aalto University, FI-00076 AALTO, Finland*

Quantum anomalies are the breaking of a classical symmetry by quantum fluctuations. They dictate how physical systems of diverse nature, ranging from fundamental particles to crystalline materials, respond topologically to external perturbations, insensitive to local details. The anomaly paradigm was triggered by the discovery of the chiral anomaly that contributes to the decay of pions into photons and influences the motion of superfluid vortices in $^3\text{He-A}$. In the solid state, it also fundamentally affects the properties of topological Weyl and Dirac semimetals, recently realized experimentally in TaAs, Na₃Bi, Cd₃As₂, and ZrTe₅. In this work we propose that the most identifying consequence of the chiral anomaly, the charge density imbalance between fermions of different chirality induced by non-orthogonal electric and magnetic fields, can be directly observed in these materials with the existing technology of photoemission spectroscopy. With angle resolution, the chiral anomaly is identified by a characteristic note-shaped pattern of the emission spectra, originating from the imbalanced occupation of the bulk states and a previously unreported momentum dependent energy shift of the surface state Fermi arcs. We further demonstrate that the chiral anomaly likewise leaves an imprint in angle averaged emission spectra, facilitating its experimental detection. Thereby, our work provides essential theoretical input to foster the direct visualization of the chiral anomaly in condensed matter.

Quantum anomalies occur when a classically preserved symmetry is broken upon quantization¹. The chiral anomaly, the first known example, refers to the non-conservation of a chiral current — a current imbalance between two distinct species of chiral fermions. Its discovery resolved the discrepancy between the measured and calculated decay rate of the neutral pion into two photons¹, and in condensed matter it was first identified as being responsible for a transverse force acting on vortices in superfluid $^3\text{He-A}$ ^{2,3}. In the solid state, Weyl and Dirac semimetals—TaAs was recently theoretically predicted^{4,5} and experimentally identified using angle-resolved photoemission spectroscopy^{6,7} (ARPES) as being a Weyl semimetal, with Na₃Bi^{8–11}, Cd₃As₂^{12–18} and ZrTe₅¹⁹ likewise identified as Dirac semimetals—are described at low energies by chiral fermions that realize a chiral anomaly and host topological surface states with Fermi arcs^{20,21}. In this work we theoretically explore the spectroscopic signatures of the chiral anomaly in these materials, with special emphasis on its effect on the Fermi arcs. We reveal an identifying note-shaped structure obtained in ARPES and a characteristic peaked structure of angular averaged photoemission spectra that allow for an experimental visualization of the chiral anomaly.

Weyl semimetals are a topological state of matter in which the conduction and valence bands touch and linearly disperse around pairs of Weyl nodes^{20,21}. Each node has a definite left or right handed chirality providing a quantum number analogous to the valley degree of freedom in graphene²². Dirac semimetals can be thought of as two superimposed copies of Weyl semimetals with the degeneracy protected by a crystal symmetry from opening up a gap^{4,5,23–25}. Similar to topological insulators and their metallic surface, Dirac and Weyl semimetals host protected surface states²⁶ that uncon-

ventionally only exist for a restricted range of crystal momenta, thereby forming a Fermi arc connecting a pair of Weyl points with opposite chirality^{26,27}. Fermi arcs have been identified with ARPES in both TaAs^{6,7} and Na₃Bi¹¹.

The chiral fermions describing the low energy degrees of freedom of Dirac and Weyl semimetals exhibit the chiral anomaly^{28–30}: while the sum of left and right handed fermions is necessarily conserved, their difference, the chiral density, does not have to be, even if classically it should. In fact, non-orthogonal magnetic and electric fields pump left handed fermions into right handed, or vice versa^{29–34}. Disorder induced internode scattering eventually counterbalances the pumping, leading to a non-equilibrium steady state with a nonzero chiral density. The chiral anomaly is theoretically predicted to result in negative magnetoresistance^{35,36} (experimentally observed in ZrTe₅¹⁹ and TaAs^{37,38}), local^{39,40} and non-local⁴¹ transport phenomena, chiral optical activity^{32,42,43} and rotation induced cooling⁴⁴.

Photoemission spectroscopy (PES) has previously been overlooked as a diagnostic tool of the chiral anomaly despite its importance in observing topological semimetals. A possible reason for this is that the finite magnetic field required to observe the chiral anomaly may complicate the disentangling of electron trajectories needed for angular resolution. Setting aside this obstacle (we return to it at the end of this work where we argue that it can be overcome) we identify the main spectral signatures of the chiral anomaly and its observable effect on the Fermi arcs. First, the bulk spectrum is determined by the differently occupied Weyl nodes distinguished by their chiralities; second, the bulk chiral imbalance tilts the Fermi arcs, which then appear at fixed energy as finite segments stemming from the bulk Fermi surface. Together, these

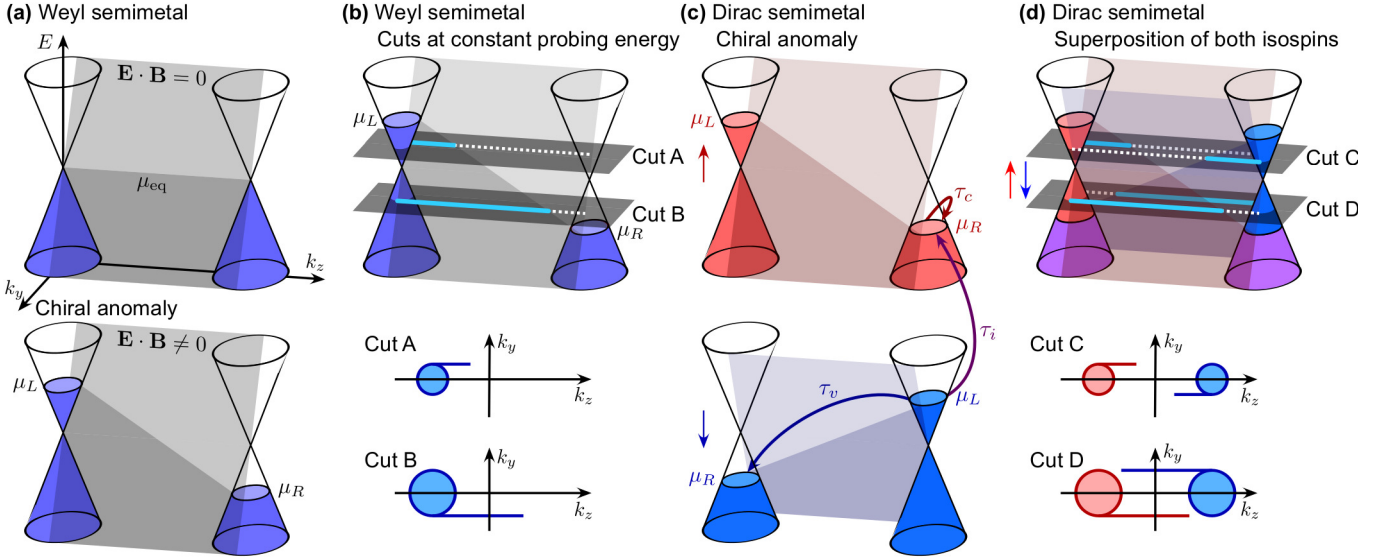


FIG. 1. **Visualization of the chiral anomaly in Dirac and Weyl semimetals.** (a) Low-energy spectrum of a Weyl semimetal film with two bulk Weyl nodes of different chirality separated in momentum space. The grey plane represents the surface state at the film's top surface, occupied up to the equilibrium chemical potential μ_{eq} . Applying external magnetic and electric fields that satisfy $\mathbf{E} \cdot \mathbf{B} \neq 0$ results in a steady state with left and right cone chemical potentials $\mu_L \neq \mu_R$, linearly interpolated by a tilted Fermi arc. (b) Two constant energy cuts (A and B) through the band structure, with occupied and empty surface states depicted by solid light blue and white dashed lines respectively. The occupation at these cuts shows a characteristic blue note-shaped pattern depicted in the lower panel. (c) Dirac semimetals host pairs of Weyl cones, each pair with fixed isospin (\uparrow or \downarrow) and both left and right chiralities, that respond to the chiral anomaly in the opposite way. Two edge states with opposite velocities (light red and light blue planes), appear at each boundary of the Dirac semimetal. Scattering processes within and between cones with scattering times τ_c , τ_v and τ_i are depicted by arrows. (d) The two pairs of Weyl nodes in (c) together comprise a pair of Dirac nodes. At a fixed energy cuts (C and D) between μ_L and μ_R , both bulk nodes are occupied while the surface states are only partially occupied. The total occupation in these planes describes two facing note-shaped patterns, illustrated in the bottom panel.

two features form a distinguishing note-shaped photoemission pattern that we argue are within reach of current experimental state of the art. We further calculate angle integrated PES, which does not suffer from the magnetic field complications of its ARPES relative, and show that distinct signatures of the chiral anomaly survive. Overall, our results supply essential theoretical input that render photoemission spectroscopy a viable probe to visualize the chiral anomaly in Dirac and Weyl semimetals.

To support our conclusions, we start by discussing the main features of the band structure of Weyl semimetals, shown in Fig. 1a. Their low-energy bulk spectrum consists of an even number of band touching points of left (L) and right (R) handed chirality that are separated in energy and momentum by breaking inversion or time-reversal symmetry. Close to the Weyl points the energy dispersion is approximately linear and described by a Weyl Hamiltonian

$$\mathcal{H}_{L/R} = \pm \hbar v \boldsymbol{\sigma} \cdot \mathbf{k}, \quad (1)$$

with \mathbf{k} the momentum, $\boldsymbol{\sigma}$ the vector of Pauli matrices and v the Fermi velocity. Its eigenstates have a spin that points either radially away from or into the Weyl point, depending on its chirality. Each Weyl node therefore acts as a monopole of Berry flux in momentum space^{3,45}. In

analogy with magnetic monopoles, a Dirac string necessarily emanates from the monopoles connecting a pair with opposite chirality⁴⁶. Any two dimensional plane in momentum space, spanned say by the two momenta k_x and k_y at a fixed k_z , that crosses the Dirac string an odd number of times and does not contain a Weyl point defines a topologically nontrivial gapped band structure. Therefore, if the system is made into a film that is finite in a real space direction conjugate to a momentum in that plane, for example either the x - or y -direction, a chiral surface state is obtained at the corresponding surfaces²⁶. Since k_z remains a good quantum number we can repeat this arguments for different planes at different k_z . Only those crossing the Dirac string odd times have a surface state, which therefore only exists for certain values of the k_z momenta. The surface state dispersion is depicted as the grey shaded plane leaning on the two Weyl nodes in Fig. 1a (the opposite surface provides an analogous surface plane with opposite velocity that is not shown). The separator between occupied and unoccupied surface states is an arc — the Fermi arc.

In the presence of non-orthogonal external electric (\mathbf{E}) and magnetic (\mathbf{B}) fields, the chiral anomaly leads to a non-conservation of the left and right handed electron densities. This is expressed by the two coupled continuity

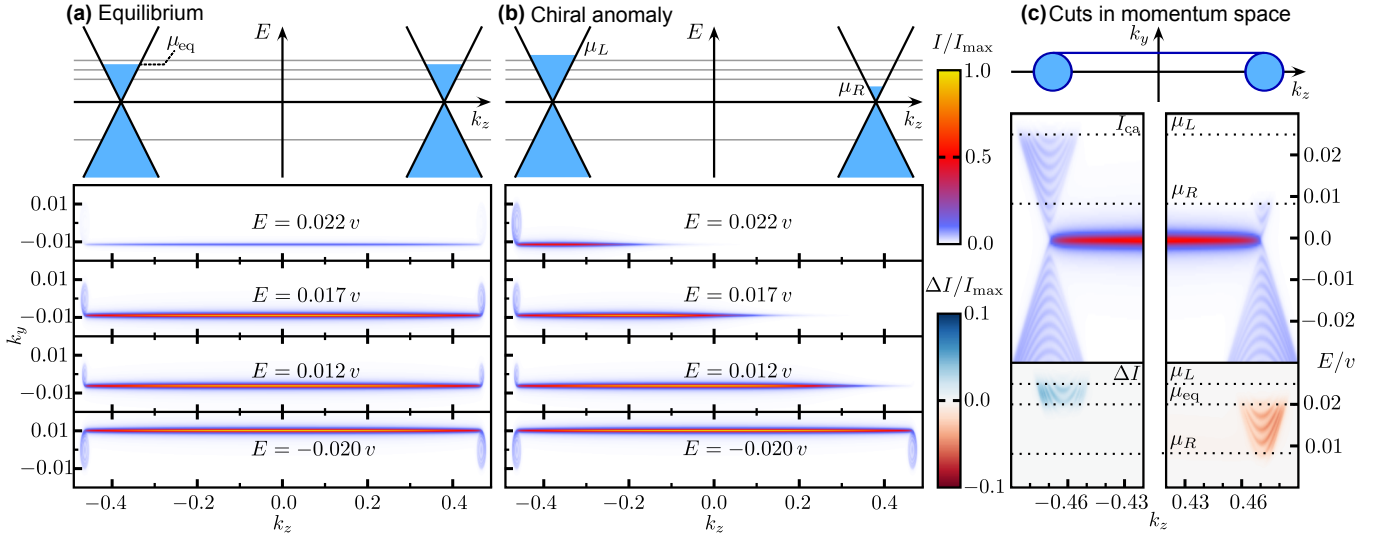


FIG. 2. **ARPES signatures of the chiral anomaly in Weyl semimetals.** Numerically computed ARPES spectra for a doped Weyl semimetal film with $L = 2000$ layers in (a) equilibrium and (b) and (c) the chiral anomaly induced steady state. The parameters are such that the equilibrium chemical potential is $\mu_{eq} = 0.02v$ while in non-equilibrium the left and right cones are filled up to $\mu_L = 0.025v$ and $\mu_R = 0.008v$ respectively. The lower panels in (a) and (b) show the momentum resolved spectra at a fixed energy, located as schematically shown with grey lines in the upper panels. In equilibrium (a), bulk cones and the surface state are observed, while the chiral anomaly (b) results in the disappearance of one cone and the emerging of the characteristic note-shaped pattern between μ_L and μ_R . The panel (c) shows the ARPES spectrum in non-equilibrium at a fixed $k_y = 0$, depicted in the top panel. The upper plot in the lower panel shows the total ARPES spectra, demonstrating the cone-like structure from the bulk and the flat surface state; the lower plot displays the intensity difference $\Delta I = I_{ca} - I_{eq}$ between the out-of-equilibrium and the equilibrium states. The dashed lines mark the chemical potentials μ_L , μ_R and μ_{eq} . These plots were obtained for $v = v_z$, $t = 0.5v$, $\epsilon = 6t$ and $b_z = 0.9v$ with the temperature set to $T = 0.001v$, which corresponds to $T \approx 5$ K for a typical Fermi velocity of $v = 0.45$ eV (see methods and supplementary material for details).

equations

$$e \partial_t n_{L/R} + \nabla \cdot \mathbf{j}_{L/R} = \mp \frac{e^3}{4\pi^2 \hbar^2} \mathbf{E} \cdot \mathbf{B} \pm \frac{e}{2\tau_v} (n_R - n_L), \quad (2)$$

where $n_{L/R}$ is the density of left and right handed fermions measured from the Weyl point and $\mathbf{j}_{L/R}$ their current density. The first term on the right hand side is the anomaly contribution, which has a different sign for the two chiralities; the second term represents the intervalley scattering with rate τ_v^{-1} . At long times, a steady state with occupation difference between the two chiralities is obtained. The continuity equations (2) and particle conservation then define the left and right handed chemical potentials

$$\mu_{L/R} = \left[\mu_{eq}^3 \mp \frac{3}{2} \hbar v^3 e^2 \tau_v \mathbf{E} \cdot \mathbf{B} \right]^{1/3}, \quad (3)$$

where μ_{eq} is the equilibrium chemical potential and we have used that $n_{L/R} = \mu_{L/R}^3 / (6\pi^2 \hbar^3 v^3)$ for three dimensional Weyl fermions. In defining $\mu_{L/R}$ we assume that the equilibration⁴⁷ within a node with intra-valley relaxation time τ_c is much shorter than the inter-valley equilibration time τ_v ⁴¹. This similarly suggests that relaxation along the surfaces is dominated by small momentum scattering such that the Fermi arc linearly interpolates in momentum space between μ_L and μ_R , analogous to the

voltage drop along an ohmic wire, leading to the steady-state occupation shown in the bottom of Fig. 1a. At a fixed energy between μ_R and μ_L this results in the characteristic note-shaped occupation schematically shown in Fig 1b for the two constant energy planes denoted cut A and cut B.

Dirac semimetals can be understood as two copies of Weyl semimetals, with each Dirac node composed of two Weyl fermions of opposite chirality. The two copies are distinguished by their different total angular momentum²⁵, which can be captured by an isospin quantum number that we denote with \uparrow and \downarrow . As long as the crystal symmetry is not broken, the isospin remains a good quantum number. This has two important consequences: one, the two chiral fermions comprising a Dirac node are decoupled and therefore a gap does not open; two, the Weyl nodes still act as monopoles in momentum space and their Dirac string connects monopoles with opposite chirality but the *same* isospin. Dirac semimetals therefore have two Fermi arcs with opposite velocity on each surface.

The two pairs of Weyl fermions in the Dirac semimetal are oppositely affected by the chiral anomaly. External and non-orthogonal \mathbf{E} and \mathbf{B} fields shift the occupation in one Dirac cone to higher energies for one isospin and to lower for the other, and oppositely in the other Dirac cone, as schematically shown in Fig. 1c. For this steady

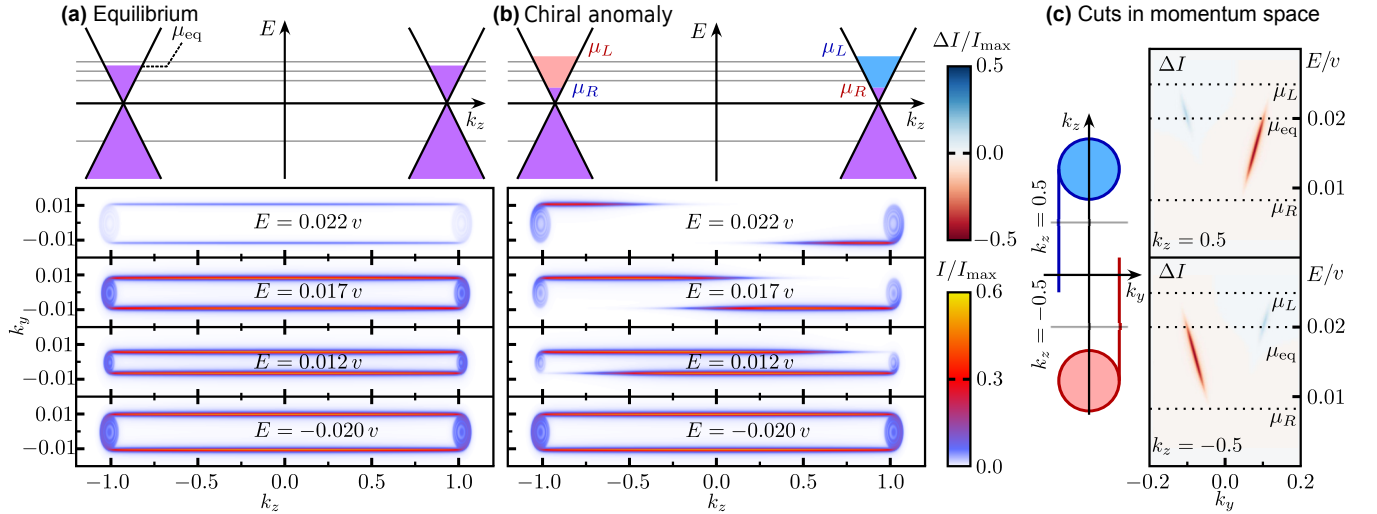


FIG. 3. **ARPES signatures of the chiral anomaly in Dirac semimetals.** Numerically computed ARPES spectra for a doped Dirac semimetal film of $L = 2000$ layers in (a) equilibrium and (b) and (c) the presence of $\mathbf{E} \cdot \mathbf{B} \neq 0$. The spectra in (a) and (b) are the momentum resolved spectra at the fixed energies schematically shown at the top as gray lines. The equilibrium chemical potential is set to $\mu_{\text{eq}} = 0.020 v$ while the left and right out of equilibrium chemical potentials are chosen to be $\mu_L = 0.025 v$ and $\mu_R = 0.008 v$. While there is a slight bulk Dirac cone intensity reduction from the equilibrium to the non-equilibrium situation, a stark qualitative difference is observed in the surface states that leads to the characteristic double note-shaped pattern. In (c) we plot the intensity difference $\Delta I = I_{\text{ca}} - I_{\text{eq}}$ for a fixed momentum $k_z = \pm 0.5$, which reveals the linear dispersion of the edge state. These plots were obtained for $M_0 = -0.2 v$, $M_1 = -0.25 v$, $M_2 = -0.75 v$ and a temperature of $T = 0.001 v$. With $v = 0.45 \text{ eV}$ for Na_3Bi , the temperature corresponds to $T \approx 5 \text{ K}$ and the induced chemical potential difference to $\delta\mu \approx 8 \text{ meV}$.

state to be realized, intra-valley relaxation at fixed chirality must be larger than both the inter-valley relaxation, $\tau_c^{-1} \gg \tau_v^{-1}$, and the intra-valley relaxation between isospins, $\tau_c^{-1} \gg \tau_i^{-1}$ (the different relaxation processes are depicted with arrows in Fig. 1c). Both conditions are estimated to be satisfied in Dirac semimetals⁴¹. Moreover, high mobility materials such as graphene satisfy the condition $\tau_c^{-1} \gg \tau_v^{-1}$, which allows for the experimental observation of a chemical potential imbalance⁴⁸ and suggests that it is also met in Cd_3As_2 .

The total occupation of a given Dirac cone is a superposition of both isospins, and therefore the bulk occupation in the chiral anomaly induced steady state is qualitatively the same as in its absence: two circular disks. In contrast, the tilt of the Fermi arcs and the resulting partial occupation at a fixed energy, see Fig. 1d, leads to a qualitatively new signature in the form of two facing note-shaped patterns (familiar from the Weyl semimetal case). This key property, which allows photoemission of Dirac semimetals to show evidence of the chiral anomaly, is a central result of our work.

We establish by a numerical computation that these note-shaped patterns are indeed directly manifested in photoemission spectra. Our simulated data is obtained with exact diagonalization of tight binding models of Weyl and Dirac semimetals, as explained in the methods section. In Fig. 2a we plot the momentum resolved ARPES spectra at various fixed energies for a doped Weyl semimetal in equilibrium. Two bulk cones and one sur-

face state at the probed surface are clearly seen; the surface state localized at the opposite surface is not visible due to the finite penetration depth of the incoming photon. In the presence of external fields $\mathbf{E} \cdot \mathbf{B} \neq 0$, the note-shaped pattern of the occupied states is seen in Fig. 2b for energies between μ_L and μ_R . An alternative way to illustrate the steady state occupation with $\mu_R \neq \mu_L$ is through a cut in momentum space at a fixed $k_y = 0$ as provided in Fig. 2c. The pumping of charge between the different chiralities is clearly revealed in the intensity difference between the equilibrium I_{eq} and chiral anomaly induced steady state I_{ca} , shown in the lower panel of Fig. 2c.

The numerically computed ARPES spectra for a Dirac semimetal, shown in Fig. 3, similarly reveal the essential features discussed in Fig. 1. In equilibrium two bulk cones and two counter-propagating edge states at the same surface are seen in Fig. 3a, similar to the experimental observations for Na_3Bi ¹¹. The non-equilibrium spectra in the presence of electric and magnetic fields are qualitatively different; two copies of the note-shaped pattern clearly reveal the chiral anomaly in Dirac semimetals. To further highlight this feature we plot, as for the Weyl semimetal, the intensity difference between the equilibrium and non-equilibrium in Fig. 3c for fixed $k_z = \pm 0.5$. The qualitatively most notable feature is the partial occupation of the surface state that results in the stem of the note. The bulk, though, is not entirely insensitive to the chiral anomaly: first, states are occupied up

to an energy $\max(\mu_L, \mu_R)$ that is higher than in the equilibrium situation; second, only one isospin band is filled between μ_L and μ_R resulting in a decreased intensity.

From the chiral anomaly equation (3) we estimate the induced chiral chemical potential difference $\delta\mu = \mu_L - \mu_R$ to be within experimental state of the art. For the doping levels of Na_3Bi , an electric field strength of 10^4 V m^{-1} and a magnetic field of 1 mT gives $\delta\mu$ of the order of 10 meV, which is well within ARPES resolution. Remarkably, magnetic fields as small as $6 \mu\text{T}$ can still achieve observable $\delta\mu \approx 2.7 \text{ meV}$ for Na_3Bi and can reach $\delta\mu \approx 5.4 \text{ meV}$ in Cd_3As_2 (details of the experimental values used to compute these estimates for different materials as well as ARPES spectra specific to Na_3Bi with curved Fermi arcs, are given in the supplementary material). The fact that experimental observation of Fermi arcs in equilibrium have already been reported also bodes well^{6,7,11}.

To achieve momentum resolution in ARPES it is necessary to correlate the angle at which an electron is detected to its initial momentum. In free space, electrons move in straight lines making this task straightforward, and a constant electric field does not overly complicate it. A magnetic field turns the electron trajectories into spirals and may, depending on the distance to the detector and size of the magnetic field, make momentum resolution difficult. However, since the magnetic field strength needed for an observable effect is rather small, correcting induced deviations is plausible⁴⁹. Alternatively, a larger uniform magnetic field finite within the sample could in principle be engineered with a ferromagnetic material in the picture frame geometry: a closed magnetic circuit that minimizes stray fields outside the sample that has been used to experimentally study ferromagnetic metals via ARPES⁵⁰ (see supplementary material for details). Similarly, if either field can be turned off fast enough (faster than the inter-valley relaxation) a pump-probe setup could observe the non-equilibrium steady state and its equilibration, which would allow for a direct measurement of the inter-valley relaxation time in addition to visualizing the chiral anomaly. While none of these are simple tasks, we believe that the rewards are significant enough that the experimental challenge will be met.

In the absence of momentum resolution the angular averaged but energy resolved photoemission spectroscopy likewise contains direct signatures of the chiral anomaly. In Fig. 4 we plot the numerically computed PES spectra as a function of energy for both Weyl and Dirac semimetals. In equilibrium it has a single step that is smeared by temperature. In the non-equilibrium steady state occupation is shifted from lower energies to higher, such that the bulk spectra would have a double step profile, with one step at μ_L and the other at μ_R . In the total spectra the two steps are hard to see since the surface states contribute significantly to smoothen the profile. The intensity difference $\Delta I = I_{\text{eq}} - I_{\text{ca}}$ instead shows a characteristic peak-dip structure for low temperatures, which reflects the chiral anomaly pumping of fermions of

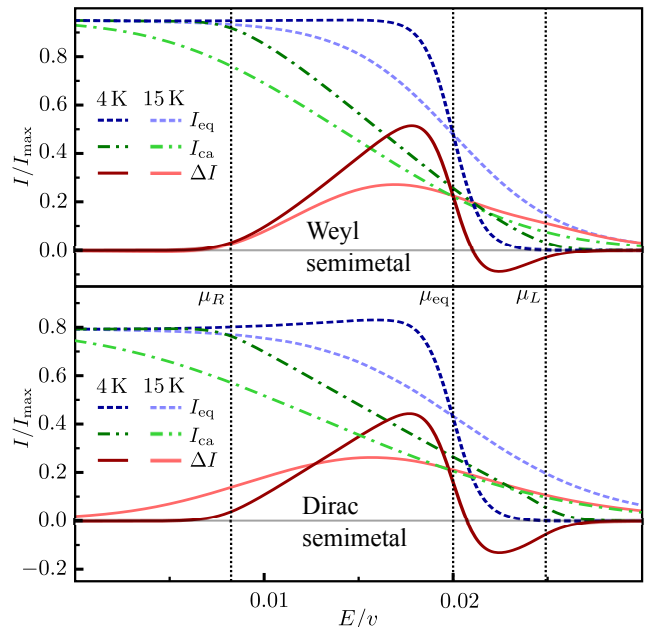


FIG. 4. Chiral anomaly in PES spectra for Dirac and Weyl semimetals. Numerically computed PES intensities for Weyl and Dirac semimetals for two different temperatures. In equilibrium the intensity I_{eq} presents a single step around μ_{eq} , that is smeared out by increasing temperature and resembles the occupation of the cones. In non-equilibrium the intensity I_{ca} shows a double-step-profile with steps at μ_R and μ_L . Both $\mu_{R/L}$ include the temperature dependence of the chiral anomaly^{2,19}. The difference $\Delta I = I_{\text{eq}} - I_{\text{ca}}$ highlights the effect of the chiral anomaly by a characteristic peak-dip structure for low temperatures, resulting from the shift in occupation of the two cones, that evolves into a single peak as temperature is increased. The parameters used to obtain these plots are $\mu_{\text{eq}} = 0.020 v$, $\mu_L = 0.025 v$, $\mu_R = 0.008 v$ at 4 K and $\mu_L = 0.024 v$, $\mu_L = 0.005 v$ at 15 K. The temperatures are chosen to be $T = 8 \cdot 10^{-4} v$ and $T = 2.9 \cdot 10^{-3} v$, corresponding to 4 K and 15 K for a typical value of $v = 0.45 \text{ eV}$. The rest of parameters are chosen as in Fig. 2 and 3 for the upper and lower panel respectively.

one chirality into the other, evolving into a single peak as temperature is increased.

In conclusion, we have promoted photoemission as an ideal tool to experimentally visualize the chiral anomaly in the solid state. The main effect that allows this is the tilt of the Fermi arc in the presence of non-orthogonal electric and magnetic fields that, through the chiral anomaly, pump electrons from one chirality to the other. As a consequence, the surface state occupation at a fixed energy no longer connects bulk nodes but rather terminates in between, resulting in a qualitatively distinct note-shaped photoemission pattern identifying the chiral anomaly. We argued, by estimating from experimentally available parameters the relevant chiral chemical potential difference to be about 10 meV, that a direct visualization of the chiral anomaly is within the state of the art. Were it to be realized experimentally in the

way proposed here, a revealing light would be shed on the relation between two fundamental concepts: quantum anomalies and topological states of matter.

METHODS

All presented ARPES spectra are calculated via exact diagonalization of tight binding Hamiltonians describing Weyl and Dirac semimetal films. For a Weyl semimetal we take

$$H_{\text{WSM}} = H_0 + H_1, \quad (4a)$$

$$H_0 = 2v(\sin k_y \sigma_x - \sin k_x \sigma_y) \tau_x + 2v_z \sin k_z \tau_y + M_{\mathbf{k}} \tau_x, \quad (4b)$$

$$H_1 = b_0 \sigma_z \tau_y + \mathbf{b} \cdot (-\sigma_x \tau_x, \sigma_y \tau_x, \sigma_z). \quad (4c)$$

The first term models a three-dimensional topological insulator⁵¹. The Pauli matrices σ and τ respectively act in spin and particle-hole space. The velocity v in the x - and y -directions differs from that in the z -direction (v_z) consistent with experimentally relevant materials. The mass $M_{\mathbf{k}} = \epsilon - 2t \sum_i \cos k_i$. At $\epsilon = 6t$ a degenerate three-dimensional Dirac cone is obtained at $\mathbf{k} = 0$. The second term⁵² breaks inversion with a nonzero b_0 and time-reversal symmetry with a finite \mathbf{b} . In our simulation we take $b_0 = 0$ and fix the direction of $\mathbf{b} = (0, 0, b_z)$ such that the Dirac cone is split into two Weyl cones at $k_z \approx \pm \frac{b_z}{2v_z}$. The low-energy spectrum of both Dirac semimetals Na_3Bi ²⁴ and Cd_3As_2 ²⁵ is modeled by the Hamiltonian

$$H_{\text{DSM}} = M_{\mathbf{k}} \sigma_z + 2v(\sin k_x \sigma_x \tau_z - \sin k_y \sigma_y), \quad (5)$$

which can be understood as two copies of two-band Weyl semimetal Hamiltonians. The mass term $M_{\mathbf{k}} = M_0 + 2M_1(\cos k_z - 1) + 2M_2(\cos k_x + \cos k_y - 2)$ sets the velocity in k_z direction to $v_z = 2\sqrt{M_0 M_1}$ and the Dirac cones to be at $k_z^c = \pm \sqrt{M_0/M_1}$. In this simple model the surface states are dispersionless in the k_z -direction.

To model a film we take the system finite in the direction orthogonal to the separation of the cones in momentum space, which is the surface where the edge states are maximally visible. The ARPES spectrum is given by an integral over the local density of states

$$I(\mathbf{k}_{\parallel}, \omega) = \int dx \sum_n |\psi_{n, \mathbf{k}_{\parallel}}(x)|^2 \delta(\epsilon_{n, \mathbf{k}_{\parallel}} - \omega) w(x) f(\omega - \mu_{\mathbf{k}_{\parallel}}), \quad (6)$$

where x is the coordinate in the finite direction of the film, $w(x) = \exp(-x/\ell)$ is a weight function modelling the incoming light's intensity decay with depth into the sample with decay length ℓ , and f is the Fermi-Dirac distribution. The wavefunctions $\psi_{n, \mathbf{k}_{\parallel}}$ are the eigenfunctions of the Hamiltonians and $\epsilon_{n, \mathbf{k}_{\parallel}}$ the corresponding eigenvalues, which depend on the momentum \mathbf{k}_{\parallel} parallel to the surface. To model the chiral anomaly induced steady state, the chemical potential $\mu_{\mathbf{k}_{\parallel}}$ is taken to be

\mathbf{k}_{\parallel} - and isospin-dependent. For the surface states, $\mu_{\mathbf{k}_{\parallel}}$ depends linearly on k_z .

ACKNOWLEDGEMENTS

We thank Sergey Borisenko, Bernd Büchner and Ilya Belopolski for useful discussions about Dirac semimetals and possible extensions of current ARPES setups, and S. Bera for helpful insights on numerical methods.

Appendix A: Aspects of experimental implementation

1. Relaxation rates

The experimental feasibility of detecting the chiral anomaly with photoemission spectroscopy relies firstly on the correct hierarchy of the different relaxation rates involved. As discussed in the main text, for Weyl semimetals the intra-valley relaxation rate at fixed chirality must be faster than the inter-valley relaxation rate, $\tau_c^{-1} \gg \tau_v^{-1}$. For Dirac semimetals it is also required that the relaxation rate between the two isospins forming each Dirac node must be shorter than the intra-valley relaxation, $\tau_i \gg \tau_c$. The intra-valley relaxation rate τ_c can be deduced from the experimental values for the carrier mobilities μ_e given in the Table I using that

$$\mu_e = \frac{\sigma}{en} = \frac{e v_F}{\hbar k_F} \tau_c, \quad (S1)$$

where σ denotes the DC conductivity, e is the electric charge, and n is the carrier density. A theoretical estimate of the ratio τ_v/τ_c can be calculated in the first Born approximation following Ref. 41, rendering the values included in the Table I that justify the assumptions used in the main text.

Experimentally, τ_v can be determined via non-local transport measurements⁴¹. The corresponding inter-valley scattering length ℓ_v was obtained experimentally in Ref. 53 for Cd_3As_2 . This length is connected to the scattering time via $\ell_v = \sqrt{D \tau_v}$, where $D = \mu_e k_B T/e$ is the charge diffusion coefficient at temperature T . Together with mobility measurements, the inter-valley scattering time τ_v at $T = 4\text{K}$ can be determined to be $\tau_v \sim 10^{-9}\text{s}$, similar to the theoretical estimate for Na_3Bi .

2. ARPES in finite magnetic fields

ARPES experiments in magnetic fields are challenging. External magnetic fields affect electron trajectories (especially those with low energies) and compromise angle resolution. Typical ARPES equipment is protected from external magnetic fields using μ -metal shields made from a metallic alloy with high magnetic permeability μ .

	Dirac Semimetals				Weyl Semimetal	
	Cd ₃ As ₂	Ref.	Na ₃ Bi	Ref.	TaAs	Ref.
μ_e (cm ² V ⁻¹ s ⁻¹)	10 ⁴ – 10 ⁵	12, 17, 18, and 54	$\sim 10^3$ –10 ⁴	55 ^a	5 · 10 ⁵	56
τ_c (s) [Eq. (S1)]	$\sim 10^{-14}$ –10 ⁻¹³		$\sim 10^{-13}$		$\sim 10^{-12}$	
τ_v/τ_c [theoretical]	-		10 ⁴	41	500	41
τ_i/τ_c [theoretical]	-		10 ³	41	τ_i not defined	
τ_v (s) [experiment]	10 ⁻⁹	53 ^b	-		-	
v ($\frac{m}{s}$)	7.6 · 10 ⁵	13	3.74 · 10 ⁵	9	3.1 – 3.6 · 10 ⁵ (W1)	37
	9.3 · 10 ⁵	16			2.6 – 4.3 · 10 ⁵ (W2)	37
	1.1 · 10 ⁶	17				
	1.3 · 10 ⁶	15				
	1.5 · 10 ⁶	12				
v_z ($\frac{m}{s}$)	$\sim 10^5$	12	2.89 · 10 ⁵	9	3.4 · 10 ⁵ (W1)	37
	3.3 · 10 ⁵	15			4.1 · 10 ⁴ (W2)	37

^a Ilya Belopolski, private communication.

^b Measurement of ℓ_v , the inter-valley relaxation time was obtained as described in the text.

TABLE I. Summary of experimentally measured Fermi velocities v and v_z , mobilities μ_e , and theoretical estimates for the relevant scattering times. For TaAs W1 (W2) nomenclature classifies the eight (sixteen) Weyl points falling on (away) the $k_z = 2\pi/c$ plane. The scattering rate τ_c is estimated for an isotropic Weyl or Dirac cone with $E_F = \hbar v k_F \sim 10$ meV.

This material offers the magnetic field lines a path with a low magnetic resistance (or reluctance) that is inversely proportional to μ , preventing them going to the energetically costly exterior. In typical ARPES experiments, for instance the set-up of Ref. 49, high resolution requires the field inside the ARPES lens to be of the order of μ T or less. In practice up to $\sim 6 \mu$ T can be handled⁴⁹. These small magnetic fields typically induce a rigid shift of the electron trajectories that can in principle be corrected⁴⁹. As we discuss in the next section, already these small fields can result in observable values of the chiral potential difference $\delta\mu \sim 4$ meV.

To allow for measurements in larger magnetic fields, without altering electron trajectories, it would be advantageous to go one step beyond existing set-ups. We suggest that a possible experimental design can be based on early ideas used to perform ARPES on ferromagnetic materials^{50,57}. Stray fields around ferromagnetic materials, like nickel, can severely alter photo-electron trajectories and jeopardize ARPES measurement accuracy. An elegant experimental solution studied these materials in the so-called picture frame geometry or remnant state^{50,57} (see Fig. 5). In this geometry, the magnetic field lines are confined within the material in a magnetic loop, minimizing their effect on electron trajectories that can spoil ARPES measurements. To reach a uniform field within a Weyl or Dirac semimetal sample, while minimizing the external stray fields, one possible solution is to open up a small gap in the magnetic circuit as shown in Fig. 5. In this set-up, a very uniform field is obtained within the gap, with possible additional fringing fields depicted as curved field lines. The effect of the fringing field is to increase the effective area of the gap, thus reducing its reluctance and increasing the effective magnetic field felt

by the sample⁵⁸. The magnitude and spatial extent of the fringing field can therefore be optimized by increasing the gap's length or cross section. In addition, if the sample cross section is designed to be slightly larger than the cross section of the gap, the fringing fields could enter the sample as well, not affecting photo-electron trajectories as shown in Fig. 5. Finally we note that external current loops were commonly used in experiments to orient the magnetization^{50,57}. Therefore it is plausible that these set-ups can admit modifications to incorporate electric fields as well.

3. Estimates of the chiral chemical potential difference

To observe the note-shaped pattern that signals the chiral anomaly it is essential that the induced chemical potential difference $\delta\mu$ is larger than the energy resolution of the experiments, which is of the order of \sim meV⁵⁹ if magnetic fields are kept of the order of $\sim \mu$ T. To estimate the difference $\delta\mu = \mu_L - \mu_R$, we use the definition of the chiral chemical potentials given by equation (3) of the main text. For the particular case where $\mu_{eq} = 0$, this difference is given by

$$\delta\mu = 2 \left(\frac{3}{2} \hbar v^2 v_z e^2 \tau_v \mathbf{E} \cdot \mathbf{B} \right)^{1/3}, \quad (\text{S2})$$

where v and v_z are the anisotropic cone Fermi velocities defined in the Methods section of the main text and reproduced in the Table I as measured by ARPES for Na₃Bi and Cd₃As₂. From Eq. (S2) we observe that it is the magnitude of the Fermi velocities, rather than τ_v or \mathbf{B} , that can most effectively enhance the chiral anomaly.

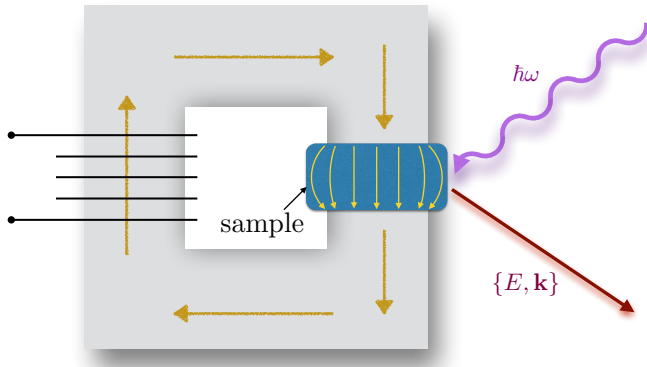


FIG. 5. Proposed magnetic circuit for studying the chiral anomaly and ARPES in a magnetic field, based on ARPES experiments on ferromagnetic materials⁵⁰. The sample is included in a magnetic circuit to minimize stray fields effects on photo-electron trajectories. The yellow arrows show the confined magnetization in the ferromagnetic material (e.g. nickel or iron) shaped into the picture-frame geometry. The Weyl or Dirac semimetal sample, a photon of energy $\hbar\omega$ and a photo-electron with energy and momentum $\{E, \mathbf{k}\}$ are depicted schematically as a blue rectangle, a purple curved arrow and a red straight arrow respectively.

To calculate $\delta\mu$ we choose two different magnetic field values $|\mathbf{B}| = 6 \mu\text{T}$ and $|\mathbf{B}| = 1 \text{ mT}$. The first corresponds to a reasonable magnetic environment that can be achieved in ARPES as discussed in the previous section, while the second is a very conservative estimate of the magnetic fields that can be achieved with the frame geometry also introduced above. All our following estimates are calculated for $|\mathbf{E}| = 1 \cdot 10^4 \text{ V m}^{-1}$. For the

relaxation rates, we choose the experimentally obtained time $\tau_v = 10^{-9} \text{ s}$ for Cd_3As_2 and the theoretical estimate $\tau_v/\tau_c = 10^4$ for Na_3Bi , both justified in Sec. A 1. These are also conservative estimates since τ_v is expected to be even larger for small chemical potentials⁴¹. Given these values, we find for Cd_3As_2 and field strengths of $|\mathbf{B}| = 1 \text{ mT}$ ($6 \mu\text{T}$) a chiral chemical potential difference of $\delta\mu \sim 30 \text{ meV}$ (5.4 meV). For Na_3Bi , we find that $\delta\mu \sim 15 \text{ meV}$ (2.7 meV) for $|\mathbf{B}| = 1 \text{ mT}$ ($6 \mu\text{T}$).

Appendix B: Case example: Na_3Bi

The main features that can lead to a direct visualization of the chiral anomaly in Weyl and Dirac semimetals via photoemission spectroscopy are presented in the main text. In order to make definite contact with current experimental state of the art, we discuss the features of the chiral anomaly for Na_3Bi . To this extent, we combine the experimental constants in Table I with parameters obtained from *ab initio* calculations for this material that define the realistic low energy model described in Ref. 24. The equilibrium ARPES spectra computed for such model, as detailed in the main text, is shown in Fig. 6(a). The figure shows a clear pair of curved Fermi arcs that connect two Dirac nodes. Distinguishing clearly these pair of arcs is well within experimental resolution, as confirmed by recent experiments [cf. Fig. 2A of Ref. 11]. Upon applying external fields that satisfy $\mathbf{E} \cdot \mathbf{B} \neq 0$, the chiral anomaly induces a chiral chemical potential difference of the order $\delta\mu \sim 10 \text{ meV}$, as estimated in the previous section. In Fig. 6(b), we show the chiral anomaly induced ARPES spectrum for Na_3Bi corresponding to such value of $\delta\mu$. The Fermi arcs are partially occupied and thus end before reaching the bulk Fermi surface, the latter not visible within this resolution. The observation of such features would directly visualize the chiral anomaly and confirm its effect on the surface electronic spectrum predicted in the main text.

¹ Bertlmann, R. A. *Anomalies in Quantum Field Theories* (Clarendon, Oxford, UK, 1996).

² Volovik, G. E. *The Universe in Helium Droplet* (Clarendon, Oxford, UK, 2003).

³ Volovik, G. E. Kopnin force and chiral anomaly. *JETP Lett.* **98**, 753–757 (2014).

⁴ Weng, H., Fang, C., Fang, Z., Bernevig, B. A. & Dai, X. Weyl semimetal phase in noncentrosymmetric transition-metal monophosphides. *Phys. Rev. X* **5**, 011029 (2015).

⁵ Huang, S.-M. *et al.* An inversion breaking Weyl semimetal state in the TaAs material class. arXiv:1501.00755.

⁶ Xu, S.-Y. *et al.* Experimental realization of a topological Weyl semimetal phase with Fermi arc surface states in TaAs. arXiv:1502.03807.

⁷ Lv, B. Q. *et al.* Discovery of Weyl semimetal TaAs. arXiv:1502.04684.

⁸ Xu, S.-Y. *et al.* Observation of a bulk 3D Dirac multiplet, Lifshitz transition, and nested spin states in Na_3Bi . arXiv:1312.7624.

⁹ Liu, Z. K. *et al.* Discovery of a Three-Dimensional Topological Dirac Semimetal, Na_3Bi . *Science* **343**, 864–867 (2014).

¹⁰ Kushwaha, S. K. *et al.* Bulk crystal growth and electronic characterization of the 3D Dirac semimetal Na_3Bi . *APL Mat.* **3** (2015).

¹¹ Xu, S.-Y. *et al.* Observation of Fermi arc surface states in a topological metal: a new type of 2D electron gas beyond \mathbb{Z}_2 topological insulators. arXiv:1501.01249.

¹² Neupane, M. *et al.* Observation of a three-dimensional topological Dirac semimetal phase in high-mobility Cd_3As_2 . *Nature Commun.* **5** (2014).

¹³ Borisenko, S. *et al.* Experimental Realization of a Three-Dimensional Dirac Semimetal. *Phys. Rev. Lett.* **113**,

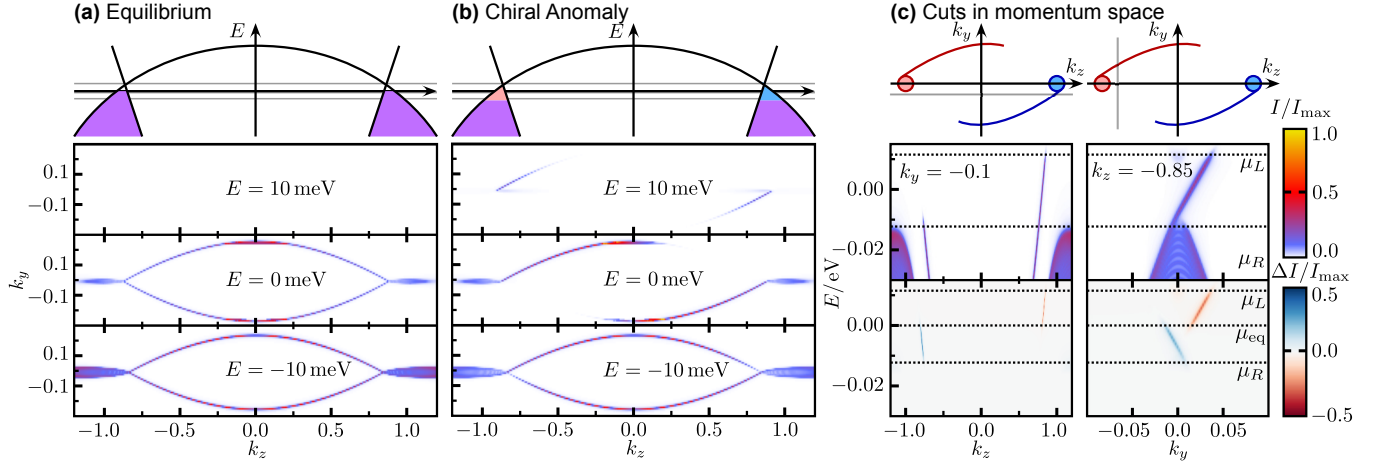


FIG. 6. **Visualization of the chiral anomaly in Na₃Bi** (a) Numerically computed equilibrium ARPES spectra for a doped Dirac semimetal film Na₃Bi with $\mu_{eq} = 0$. The pair of Fermi arcs are well within experimental energy and momentum resolution, confirmed by the recent experiment Ref. 11. (b) Chiral anomaly induced ARPES spectra for the same material and an estimate of the chiral chemical potential difference $\delta\mu \approx 20$ meV derived in section A. The Fermi arcs show evidence of partial occupation within experimental resolution. The upper panels in (a) and (b) show a schematic representation of the bulk band structure with two Dirac nodes connected at higher energies. (c) The lower panel shows two cuts through momentum space at $k_y = -0.1$ and $k_z = -0.85$ in units of the lattice constants and represented schematically by the horizontal and vertical light grey lines in the upper panel. The parameters of the low energy model used to obtain these figures are extracted from first principles in Ref. 24 and take the values $v = 0.45$ eV, $M_0 = -0.087$ eV, $M_1 = -0.11$ eV, $M_2 = -0.35$ eV and $C_0 = -0.064$ eV, $C_1 = 0.094$ eV, $C_2 = -0.28$ eV. All calculations were performed at a temperature of $T = 1$ meV = 11.6 K and for a film thickness of $L = 1000$ layers.

- 027603 (2014).
- ¹⁴ Yi, H. *et al.* Evidence of Topological Surface State in Three-Dimensional Dirac Semimetal Cd₃As₂. *Sci. Rep.* **4** (2014).
 - ¹⁵ Liu, Z. K. *et al.* A stable three-dimensional topological Dirac semimetal Cd₃As₂. *Nat. Mater.* **13**, 677–681 (2014).
 - ¹⁶ Liang, T. *et al.* Ultrahigh mobility and giant magnetoresistance in the Dirac semimetal Cd₃As₂. *Nat. Mater.* **14**, 280–284 (2015).
 - ¹⁷ He, L. P. *et al.* Quantum Transport Evidence for the Three-Dimensional Dirac Semimetal Phase in Cd₃As₂. *Phys. Rev. Lett.* **113**, 246402 (2014).
 - ¹⁸ Feng, J. *et al.* Large linear magnetoresistance in Dirac semi-metal Cd₃As₂ with Fermi surfaces close to the Dirac points. arXiv:1405.6611.
 - ¹⁹ Li, Q. *et al.* Observation of the chiral magnetic effect in ZrTe₅. arXiv:1412.6543.
 - ²⁰ Turner, A. M. & Vishwanath, A. Beyond band insulators: topology of semi-metals and interacting phases. arXiv:1301.0330.
 - ²¹ Hosur, P. & Qi, X. Recent developments in transport phenomena in Weyl semimetals. *C. R. Phys.* **14**, 857–870 (2013).
 - ²² Castro Neto, A. H., Guinea, F., Peres, N. M. R., Novoselov, K. S. & Geim, A. K. The electronic properties of graphene. *Rev. Mod. Phys.* **81**, 109–162 (2009).
 - ²³ Young, S. M. *et al.* Dirac Semimetal in Three Dimensions. *Phys. Rev. Lett.* **108**, 140405 (2012).
 - ²⁴ Wang, Z. *et al.* Dirac semimetal and topological phase transitions in A₃Bi (A = Na, K, Rb). *Phys. Rev. B* **85**, 195320 (2012).
 - ²⁵ Wang, Z., Weng, H., Wu, Q., Dai, X. & Fang, Z. Three-dimensional Dirac semimetal and quantum transport in Cd₃As₂. *Phys. Rev. B* **88**, 125427 (2013).
 - ²⁶ Wan, X., Turner, A. M., Vishwanath, A. & Savrasov, S. Y. Topological semimetal and Fermi-arc surface states in the electronic structure of pyrochlore iridates. *Phys. Rev. B* **83**, 205101 (2011).
 - ²⁷ Xu, G., Weng, H., Wang, Z., Dai, X. & Fang, Z. Chern Semimetal and the Quantized Anomalous Hall Effect in HgCr₂Se₄. *Phys. Rev. Lett.* **107**, 186806 (2011).
 - ²⁸ Nielsen, H. & Ninomiya, M. The Adler-Bell-Jackiw anomaly and Weyl fermions in a crystal. *Phys. Lett. B* **130**, 389–396 (1983).
 - ²⁹ Volovik, G. E. On induced CPT-odd Chern-Simons terms in the 3+1 effective action. *JETP Lett.* **70**, 1–4 (1999).
 - ³⁰ Aji, V. Adler-Bell-Jackiw anomaly in Weyl semimetals: Application to pyrochlore iridates. *Phys. Rev. B* **85**, 241101 (2012).
 - ³¹ Zyuzin, A. A. & Burkov, A. A. Topological response in Weyl semimetals and the chiral anomaly. *Phys. Rev. B* **86**, 115133 (2012).
 - ³² Grushin, A. G. Consequences of a condensed matter realization of Lorentz-violating QED in Weyl semi-metals. *Phys. Rev. D* **86**, 045001 (2012).
 - ³³ Goswami, P. & Tewari, S. Axionic field theory of (3+1)-dimensional Weyl semimetals. *Phys. Rev. B* **88**, 245107 (2013).
 - ³⁴ Liu, C.-X., Ye, P. & Qi, X.-L. Chiral gauge field and axial anomaly in a Weyl semimetal. *Phys. Rev. B* **87**, 235306 (2013).
 - ³⁵ Abrikosov, A. A. Quantum magnetoresistance. *Phys. Rev. B* **58**, 2788–2794 (1998).
 - ³⁶ Son, D. T. & Spivak, B. Z. Chiral anomaly and classical negative magnetoresistance of Weyl metals. *Phys. Rev. B* **88**, 104412 (2013).

- ³⁷ Huang, X. *et al.* Observation of the chiral anomaly induced negative magneto-resistance in 3D Weyl semi-metal TaAs. arXiv:1503.01304.
- ³⁸ Zhang, C. *et al.* Observation of the Adler-Bell-Jackiw chiral anomaly in a Weyl semimetal. arXiv:1503.02630.
- ³⁹ Landsteiner, K. Anomalous transport of Weyl fermions in Weyl semimetals. *Phys. Rev. B* **89**, 075124 (2014).
- ⁴⁰ Zhou, J., Chang, H.-R. & Xiao, D. Plasmon mode as a detection of the chiral anomaly in Weyl semimetals. *Phys. Rev. B* **91**, 035114 (2015).
- ⁴¹ Parameswaran, S. A., Grover, T., Abanin, D. A., Pesin, D. A. & Vishwanath, A. Probing the Chiral Anomaly with Nonlocal Transport in Three-Dimensional Topological Semimetals. *Phys. Rev. X* **4**, 031035 (2014).
- ⁴² Hosur, P. & Qi, X.-L. Tunable optical activity due to the chiral anomaly in Weyl semimetals. arXiv:1401.2762.
- ⁴³ Ashby, P. E. C. & Carbotte, J. P. Chiral anomaly and optical absorption in Weyl semimetals. *Phys. Rev. B* **89**, 245121 (2014).
- ⁴⁴ Başar, G., Kharzeev, D. E. & Yee, H.-U. Triangle anomaly in Weyl semimetals. *Phys. Rev. B* **89**, 035142 (2014).
- ⁴⁵ Vafeek, O. & Vishwanath, A. Dirac fermions in solids: from high- T_c cuprates and graphene to topological insulators and Weyl semimetals. *Annu. Rev. Condens. Matter Phys.* **5**, 83–112 (2014).
- ⁴⁶ Dirac, P. A. M. Quantized Singularities in the Electromagnetic Field. *Proc. R. Soc. A* **133**, 60–72 (1931).
- ⁴⁷ The definition of the relaxation times includes energy relaxation processes at small momenta, which we assume happen on a timescale shorter than any elastic scattering.
- ⁴⁸ Gorbachev, R. V. *et al.* Detecting topological currents in graphene superlattices. *Science* **346**, 448–451 (2014).
- ⁴⁹ Enderlein, C. *Graphene and its interaction with different substrates studied by angular-resolved photoemission spectroscopy*. Ph.D. thesis, Freie Universität, Berlin (2010).
- ⁵⁰ Raue, R., Hopster, H. & Clauberg, R. Observation of spin-split electronic states in solids by energy-, angle-, and spin-resolved photoemission. *Phys. Rev. Lett.* **50**, 1623–1626 (1983).
- ⁵¹ Qi, X.-L. & Zhang, S.-C. Topological insulators and superconductors. *Rev. Mod. Phys.* **83**, 1057–1110 (2011).
- ⁵² Vazifteh, M. M. & Franz, M. Electromagnetic Response of Weyl Semimetals. *Phys. Rev. Lett.* **111**, 027201 (2013).
- ⁵³ Zhang, C. *et al.* Detection of chiral anomaly and valley transport in Dirac semimetals. arXiv:1504.07698.
- ⁵⁴ Jay-Gerin, J.-P., Aubin, M. & Caron, L. The electron mobility and the static dielectric constant of Cd_3As_2 at 4.2 K. *Solid State Communications* **21**, 771–774 (1977).
- ⁵⁵ Xiong, J. *et al.* Anomalous conductivity tensor in the Dirac semimetal Na_3Bi . arXiv:1502.06266.
- ⁵⁶ Zhang, C. *et al.* Tantalum monoarsenide: an exotic compensated semimetal. arXiv:1502.00251.
- ⁵⁷ Donath, M. Spin-dependent electronic structure at magnetic surfaces: The low-miller-index surfaces of nickel. *Surface Science Reports* **20**, 251 – 316 (1994).
- ⁵⁸ Becherrawy, T. *Electromagnetism: Maxwell Equations, Wave Propagation and Emission* (John Wiley and Sons, 2012).
- ⁵⁹ Liu, G. *et al.* Development of a vacuum ultraviolet laser-based angle-resolved photoemission system with a super-high energy resolution better than 1meV. *Review of Scientific Instruments* **79** (2008).